The Astrophysical Journal Letters, 934:L25 (7pp), 2022 August 1 https://doi.org/10.3847/2041-8213/ac822b

Water Shielding in the Terrestrial Planet-forming Zone: Implication for Inner Disk Organics

Sara E. Duval, Arthur D. Bosman, and Edwin A. Bergin
University of Michigan, LSA Astronomy, 1085 S. University Avenue, Ann Arbor, MI 48109, USA; saraduval018@gmail.com
Received 2022 June 9; revised 2022 July 8; accepted 2022 July 17; published 2022 July 29

Abstract

The chemical composition of the inner region of protoplanetary disks can trace the composition of planetary-building material. The exact elemental composition of the inner disk has not yet been measured and tensions between models and observations still exist. Recent advancements have shown UV shielding to be able to increase the emission of organics. Here, we expand on these models and investigate how UV shielding may impact chemical composition in the inner 5 au. In this work, we use the model from Bosman et al. and expand it with a larger chemical network. We focus on the chemical abundances in the upper disk atmosphere where the effects of water UV shielding are most prominent and molecular lines originate. We find rich carbon and nitrogen chemistry with enhanced abundances of C_2H_2, CH_4, HCN, CH_3CN, and NH_3 by >3 orders of magnitude. This is caused by the self-shielding of H_2O, which locks oxygen in water. This subsequently results in a suppression of oxygen-containing species like CO and CO_2. The increase in C_2H_2 seen in the model with the inclusion of water UV shielding allows us to explain the observed C_2H_2 abundance without resorting to elevated C/O ratios as water UV shielding induced an effectively oxygen-poor environment in oxygen-rich gas. Thus, water UV shielding is important for reproducing the observed abundances of hydrocarbons and nitriles. From our model result, species like CH_4, NH_3, and NO are expected to be observable with the James Webb Space Telescope (JWST).

Unified Astronomy Thesaurus concepts: Protoplanetary disks (1300); Astrochemistry (75); Chemical abundances (224)

1. Introduction

Within protoplanetary disks, the inner 2 to 3 au is a critical location where much of the process of planet formation is believed to occur, referred to as the planet-forming zone (e.g., Pierrehumbert & Gaidos 2011; Morbidelli et al. 2012; Raymond et al. 2014; Morbidelli & Raymond 2016). Most directly, this region corresponds to radii at which terrestrial planets are formed (Mulders et al. 2015; Madhusudhan et al. 2021). Observations have shown that many stars are expected to have a planet within 1 au (Johnson et al. 2010; Mulders et al. 2018). The inner 1 au is inside or contains the H_2O ice line and water plays a large role in the evolution of life (e.g., Brown et al. 2013; Cockell et al. 2016; Lingam & Loeb 2019). Furthermore, inside the water-ice line, the elemental C/O ratio is predicted to be ∼stellar, which becomes inherited by giant planets (Öberg et al. 2011; Ida et al. 2019; Öberg et al. 2021). Thus, the location of formation impacts chemical composition (e.g., Lahuis et al. 2006; Öberg et al. 2011; Pontoppidan et al. 2011; Walsh et al. 2012; Madhusudhan 2019).

The inner disk is dust rich, leading to high optical depths. This makes it difficult to determine the chemical content of the disk midplane. However, the radiation from the star, which is in close proximity, leads to a heated disk surface (i.e., $T_{\rm gas} > T_{\rm dust}$), which produces a rich spectrum of emission from volatile molecules, particularly at infrared wavelengths (e.g., Carr & Najita 2008; Brown et al. 2013). Water vibrational lines at 3 μm, HCN vibrational at 3.3 μm, and CO vibrational at 4.7 μm have been observed with both Keck Near Infrared Spectrograph (NIRSPEC) and VLT-CRIRES (e.g., Salyk et al. 2011a; Brown et al. 2013; Mandell et al. 2013; Carr et al. 2018). Further lines of H_2O, OH, HCN, C_2H_2, and CO_2 have been detected by the Spitzer Space Telescope Infrared Spectrograph (IRS), which ranges from 10 to 37 μm (e.g., Carr & Najita 2008; Salyk et al. 2008, 2011b; Pontoppidan et al. 2010). All of these lines are thought to originate in the inner 2 to 3 au, which allows us to trace the gas composition. These observations show that diverse chemistry is present in the inner planet-forming zone.

Najita et al. (2013, 2018) investigate the ratio of HCN/H_2O line flux and find it is related to disk dust mass. They argue that this relation is due to the formation of planetesimals that decouple from the dust and lock up water in distant regions. This effectively increases the C/O ratio in the inner disk, directly impacting the HCN/H_2O line flux. Banzatti et al. (2020) explore the same data set and find that the strongest relation is an anticorrelation between L_{H_2O} and $R_{\rm dust}$. Instead of an elevated C/O, they propose that the inner disk is fed by drifting pebbles, where large disks are a sign of little drift and small disks are a sign of substantial drift. Because these pebbles are water-ice rich, a high drift rate will enhance the inner disk oxygen content when the water ice sublimates. To distinguish these scenarios, we need to understand the C/O ratio of inner disk gas.

One way to determine the inner disk chemical content and C/O ratio is to use detailed thermochemical models. Models such as Dust and LInes (DALI) (Bruderer et al. 2012; Bruderer 2013), RAC2D (Du & Bergin 2014), and Protoplanetary Disk Model (ProDiMo) (Woitke et al. 2009) solve for both the gas thermal physics and the chemical equilibrium, given stellar parameters, the dust properties and mass distribution, and an overall gas-to-dust mass ratio. Based on these models,

Woitke et al. (2018) and Anderson et al. (2021) find that altering the C/O ratio changes the predicted emission of molecules arising from inner disk gas. In their models, they have matched emission from multiple organics but underproduced C_2H_2 unless an elevated C/O ratio is invoked.

Bethell & Bergin (2009) showed that strong formation rates of water vapor in hot (>400 K) surface gas can compete with ultraviolet (UV) photodestruction, allowing water to self-shield. Because water has a broad UV photoabsorption cross section (Yoshino et al. 1996), this can also shield other molecules downstream, a process called water UV shielding. Bosman et al. (2022a, hereafter Paper I), Calahan et al. (2022, hereafter Paper II), and Bosman et al. (2022b, hereafter Paper III) have shown that water UV shielding lowers the UV flux deeper into the disk and is important in understanding H_2O, $H_2^{18}O$, and CO_2 emission.

Additional species beyond H_2O, such as H_2, CO, C I, H I, and N_2, are also abundant in the surface layers to potentially impact the UV field. H_2, CO, atomic carbon, and N_2 all absorb wavelengths less than 110 nm, while most other species dissociate at wavelengths >110 nm and most of the UV photons are also in this wavelength range (e.g., Herczeg et al. 2004; Heays et al. 2017). Thus, while the UV attenuation of these species greatly impacts each other, they do not greatly impact the dissociation of other species, in contrast to H_2O. Shielding by atomic H, specifically scattering of Lyα, does not seem to have a big impact on the chemistry of the inner disk (Paper II).

This naturally raises the question as to whether water UV shielding affects the rest of the chemistry in the inner disk. This is what we investigate in this paper: the impact of water UV shielding on chemistry in the inner disk, with the goal of reconciling current models with observations and making predictions for observations with the James Webb Space Telescope.

2. Methods

2.1. Model Setup

We use the DALI models from Paper I. These models include modifications from standard DALI (Bruderer et al. 2012; Bruderer 2013) to better represent the inner disk regions. These include more efficient H_2 formation at high temperatures, more efficient heating following photodissociation (following Glassgold & Najita 2015), and water UV shielding (Bethell & Bergin 2009, Paper I). The models have an AS 209–like input spectrum, with most of the UV in Lyα taken from Zhang et al. (2021). Model setup details are in Paper I, and model parameters are reiterated in Table 1. For this Letter, we will only focus on one of the four structures discussed in Paper I, the flat ($h_c = 0.08$) model with a gas-to-dust ratio of 10^5, as this model is best able to reproduce both the water and CO_2 emission (Paper III). The elemental abundances assumed in the chemistry are found in Table 1 and are based on Jonkheid et al. (2006), with reduced Mg, Si, S, and Fe. Finally, as the chemical timescale in the region of interest is short, we solve for statistical equilibrium (Anderson et al. 2021).

The DALI models use a simplified chemical network, which is sufficient for species such as CO, H_2O, and CO_2. However, it does not include the reactions for realistic abundances of the organics, including C_2H_2 and HCN, which have been commonly observed with Spitzer-IRS (Carr & Najita 2008; Pontoppidan et al. 2010). To correct this, we use an expanded chemical network. This network is based on the network from Walsh et al. (2015) and includes modifications as noted in Bosman et al. (2021). Furthermore, we made sure that the adaptations made to the simplified network, such as the H_2 formation reactions, three-body reactions, and the collisional dissociation reactions are correctly incorporated into the bigger chemical network. This chemical network is then used to calculate the chemical composition with the gas temperature and UV field from the standard DALI model. We adopt the H_2O abundances from the full chemical calculation to calculate the shielding of UV photons for the chemistry, but we do not update the gas temperature. More details on the model setup can be seen in the Appendix. Figure 4 contains information about the disk structure for our UV-shielding model. In Figure 5, we show that the water abundances between the simplified and full network are very similar in the surface layers where water UV shielding is most important.

Table 1
Disk Model Parameters

Parameter	Value
Stellar luminosity	1 $L_\odot$
Stellar spectrum	AS 209 [a]
Stellar mass	1.0$M_\odot$
X-ray luminosity	10^{30} erg s^{-1}
Cosmic-ray ionization rate	10^{-17} s^{-1}
Sublimation radius	0.08 au
Critical radius	46 au
Disk outer radius	100.0 au
Gas surf. dens. at R_c	21.32 g cm^{-2}
Surf. dens. power-law slope	0.9
Disk-opening angle	0.08
Disk-flaring angle	0.11
Large dust fraction	0.999
Large dust settling	0.2
Element	**Abundance w.r.t. H**
H	1.0
He	7.59×10^{-2}
C	1.35×10^{-4}
N	2.14×10^{-5}
O	2.88×10^{-4}
Mg	4.17×10^{-9}
Si	7.94×10^{-8}
S	1.91×10^{-8}
Fe	4.27×10^{-9}

2.2. Determination of the Emitting Layer

In Paper I, hot (>300–400 K) water vapor is found in high abundance in a thin surface layer that is radially confined within 1 au. In this region, the water vapor column exceeds 10^{20} cm^{-2} and with a gas-to-dust ratio of 10^5, dust UV absorption is negligible compared to water UV shielding. Thus, including water shielding alters the UV transfer on the surface of the disk, which should lead to large differences in our models. In the disk surface, UV photons heat the gas, creating $T_{\rm gas} > T_{\rm dust}$, a condition necessary for the emission of molecular lines. The inclusion of UV shielding thus is expected to lower the gas temperature and decrease emission deeper in the disk. This provides a boundary from below which we do not expect emission. In Papers I–III, we found that the emission comes from gas of $T_{\rm gas} \gtrapprox$ 300–400 K and a hydrogen nuclei

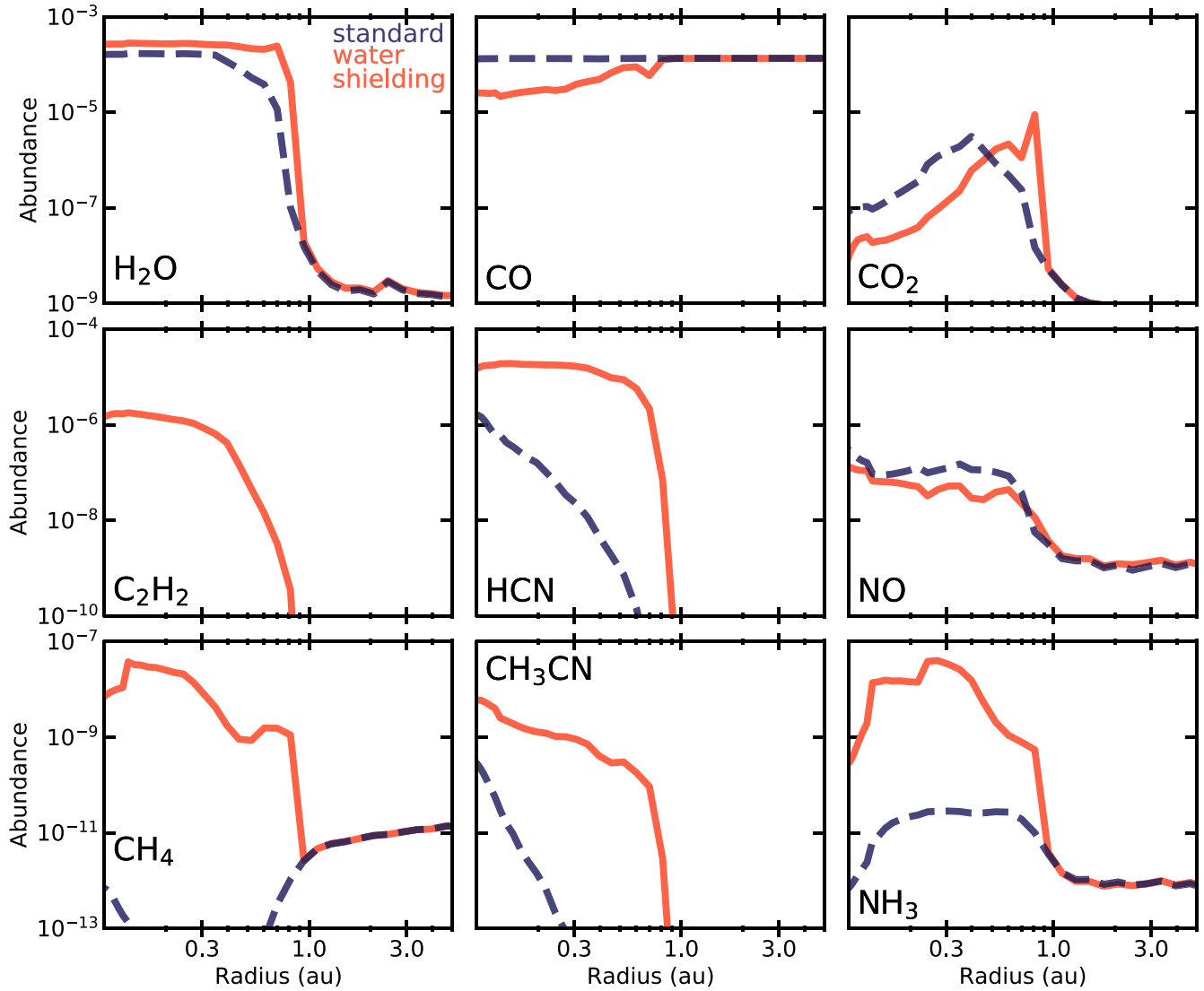

Figure 1. The molecular abundance of various species over the inner 5 au, determined from the IR-emitting layer, for the standard and water-shielding models. The locations of the water and CO_2 ice lines are at 0.27 and 0.94 au, respectively. The drops in abundance near 0.9 au are a result of drops in the gas temperature in the surface layer (see Section 4).

column of $\lesssim 10^{24}$ cm^{-2}. This paper does not explore the radiation transfer, so we consider the top 10^{24} cm^{-2} as our "infrared (IR)-emitting layer", corresponding to a $z/r \gtrsim 0.15$, and focus our analysis on the chemical composition of this layer.

3. Results

Figure 1 shows the abundance in the emitting layer for two models, with and without water UV shielding (water shielding and standard, respectively). For H_2O, the predicted abundance remains relatively similar at radii within the CO_2 ice line, where the model with UV shielding has more abundant water. In the case of CO, there is a clear depletion in abundance for the model with water UV shielding. On the disk surface, CO can be destroyed by two pathways. In the highest reaches where CO is not fully shielded, it can be directly dissociated by UV radiation or through reactions with He^+, which requires ionization by X-rays. Both pathways create free oxygen which is stolen to make H_2O before CO can re-form. In summary, the important reaction pathway is

$$\begin{aligned} &CO + h\nu \rightarrow C + O \\ &He^+ + CO \rightarrow C^+ + O + He \\ &O + H_2 \rightarrow OH + H \\ &OH + H_2 \rightarrow H_2O + H, \end{aligned} \quad (1)$$

which leaves carbon without any oxygen to re-form CO. This excess carbon is sequestered in large (hydro)carbon-chain species, which will be discussed in Section 4.1.

The behavior of CO_2 varies with radius. In the inner 1 au, the progressively lower temperature at increasing radius increases the CO_2 formation rate relative to the water formation rate (e.g., Bosman et al. 2018). Outside of the CO_2 midplane ice line, the temperatures of the surface layers become too low for the efficient formation of OH, the main precursor of CO_2, causing a strong CO_2 abundance drop. H_2O, C_2H_2, HCN, NO, CH_4, CH_3CN, and NH_3 all experience a similar temperature-driven drop in abundance around 0.9 au.

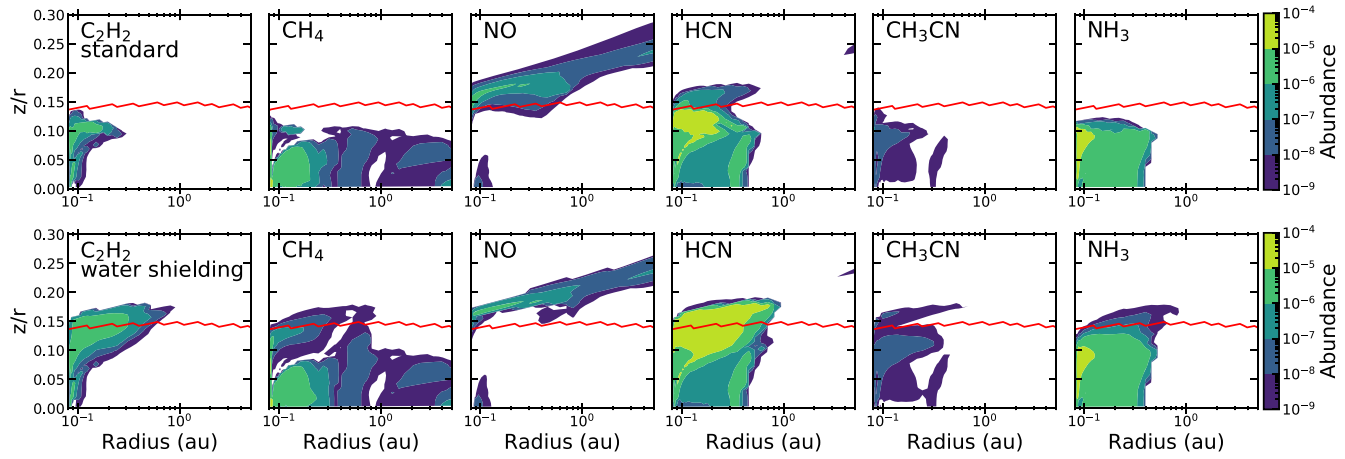

Figure 2. The 2D abundance distributions of the six species for the standard and water-shielding models in the inner 5 au. The red line signifies the location of our estimate of the IR-emitting layer above $z/r \sim 0.15$. It is clear that with the inclusion of water UV shielding, these species reach higher abundances at locations higher up in the disk atmosphere.

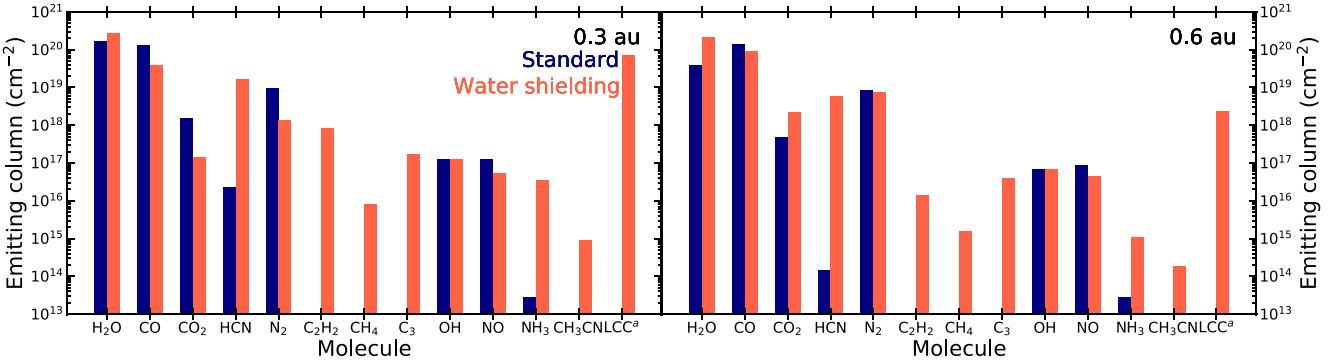

Figure 3. Abundant gas-phase species for the standard and water-shielding models at 0.3 au and 0.6 au. C_2H_2, CH_4, C_3, CH_3CN, and LCC have abundances below 10^{12} cm^{-2} for the standard model. It should be noted that at 0.6 au, there is a higher abundance of LCC in ice form. (LCC signifies large carbon chains containing four or more carbons).

We have selected a number of species that have many orders of magnitude difference in abundance, between the standard model and including water UV shielding, out to the CO_2 ice line: C_2H_2, HCN, CH_4, CH_3CN, and NH_3. For these species, water UV shielding has a significant effect, enhancing these abundances by >3 orders of magnitude, in disks with high gas-to-dust mass ratios, where there is significant dust settling and growth. We expect that the species with an enhanced abundance due to water UV shielding will be able to be observed more prominently at heights farther up in the disk atmosphere. Figure 3 shows the emitting columns for these species at 0.3 and 0.6 au along with the other abundant species that are present in our UV-shielded model. It can be seen that the impact of UV shielding on molecular abundance yields significant results, impacting abundance at radii less than 0.9 au.

Figure 2 shows the 2D abundance distributions for the standard model and the water-shielding model over the inner 5 au for C_2H_2, CH_4, NO, HCN, CH_3CN, and NH_3. Looking at the IR-emitting layer, the area above the red line at $z/r \sim 0.15$, it is clear that this region is most affected by the inclusion of water UV shielding. We see that C_2H_2, CH_4, CH_3CN, and NH_3 are found in the IR-emitting layer only if water UV shielding is included, while NO becomes depleted relative to the standard model, as was found in the average abundances in Figure 1. At deeper layers, below the IR-emitting layer, practically identical results are seen for both models, reflecting how the differences in abundance are limited to the surface layers. Thus, Figure 1 includes the entire vertical column of gas that is impacted by UV shielding.

4. Discussion

4.1. Carbon

In Figure 1, the CO abundance is reduced within the CO_2 ice line when water UV shielding is included. The self-shielding of water lowers the abundance of water photoproducts, such as atomic oxygen and OH, in the gas. These species are critical in the formation of CO, so its formation is slowed. This effect, combined with dissociation reactions with He^+ in the upper atmosphere as discussed in Section 3, reduces the abundance of CO. Thus, more carbon is available for the formation of other species.

Similarly to CO, we can also see that the abundance of CO_2 is reduced when water self-shielding is included due to atomic oxygen and OH-poor environment (Bosman et al. 2022b); both are crucial to its formation. In contrast, we see increases in abundance for HCN, C_2H_2, CH_4, and CH_3CN.

Figure 3 shows that at 0.3 au, most of the carbon is incorporated into long carbon chains, such as C_6H_2 and C_9H_2 for the UV-shielding model with abundances of 3×10^{-6} (relative to total H). This result is similar to Wei et al. (2019), who explore releases of carbon from refractory carbon-rich grains. They find the efficient creation of large carbon-chain species if carbon grain destruction is included. Though there

are differences in the origin of the carbon chains between Wei et al. (2019) and our models, the similar end results suggest that inner disk chemistry drives large carbon-chain production whenever there is little atomic oxygen available.

Past models by Woitke et al. (2018) and Anderson et al. (2021) have found low abundances and fluxes of C_2H_2. In their models, matching observation and theory requires a high C/O ratio, thus creating an inability to reproduce H_2O observations. Figure 1 shows that the C_2H_2 abundance is elevated in an effectively oxygen-poor environment, as created by UV shielding in gas that is oxygen rich (i.e., stellar O/H in content). As $T_{\rm gas} > T_{\rm dust}$ in this region, this should lead to a strong increase in 13.7 μm C_2H_2 emission. At 0.3 au, our models produce a C_2H_2 column density of 8.4×10^{17} cm^{-2} in the region of the disk in the IR-emitting layer. The models of Anderson et al. (2021) have found the column density of C_2H_2 to be in the range of $10^{14}-10^{16}$ cm^{-2}, and Woitke et al. (2018) found it to be equal to 10^{17} cm^{-2} for a C/O ratio of 0.46. It should be noted that most of this column is at a low gas temperature of 230K and thus only weakly contributes to any line emission. Our models thus produce a larger amount of C_2H_2 in higher regions of the disk without invoking an elevated C/O ratio.

Compared to the observations of Salyk et al. (2011b), they find best-fit columns on the order of $10^{14}-10^{15}$ cm^{-2} for C_2H_2. This is low compared to our value of 10^{18} cm^{-2} at 0.3 au. This discrepancy could be explained by the way the column is derived in Salyk et al. (2011b), in which the emitting area for water was determined and applied to all species. The region in which C_2H_2 has a high abundance is smaller than that of water, so it is expected that the C_2H_2-emitting region is smaller as well. This smaller emitting region would also imply a C_2H_2 excitation temperature that is higher than that of H_2O, as is seen in Salyk et al. (2011b). If the actual emitting region of C_2H_2 is smaller than assumed in the fitting by Salyk et al. (2011b), then the column will have to be decreased significantly to compensate and still produce the same total flux. This could explain the mismatch between the observation-derived columns and our predicted columns.

Finally, it is important to note the carbon species that we expect to see in this region. We likely expect to observe CH_4 with a column of 8×10^{15} cm^{-2} at 0.3 au. High abundances of C_3 and long carbon chains with low hydrogenation are seen in Figure 3, which indicates that these species could have detectable band emission. It is unlikely to detect C_2H_6 and C_2H_4 in this region as the models produced columns of less than 6×10^{13} cm^{-2} and 2×10^{14} cm^{-2}, respectively.

4.2. Nitrogen

Water UV shielding has a strong effect on the nitrogen-bearing species, increasing abundances of HCN, NH_3, and CH_3CN while lowering the abundance of NO. The abundance of HCN is known to be sensitive to the gas-phase C/O ratio (e.g., Cleeves et al. 2018). Our model effectively changes the C/O ratio and, thus, HCN rises in abundance for the water UV-shielding model. This is in large part driven by the chemistry discussed in Section 4.1. However, the changes in NH_3 and NO imply that the active nitrogen chemistry is also changed.

There seem to be three driving factors for the increased abundance of NH_3, HCN, and CH_3CN. The first driving factor is due to an impediment placed within the formation pathway of N_2. N_2 is primarily formed from atomic N by the reactions

$$\begin{aligned} \mathrm{N} + \mathrm{OH} &\rightarrow \mathrm{NO} + \mathrm{H} \\ \mathrm{NO} + \mathrm{N} &\rightarrow \mathrm{N_2} + \mathrm{O}. \end{aligned} \quad (2)$$

With the inclusion of water self-shielding, the OH abundance is lowered, and this channel is suppressed. Further, in both the standard and full models, N_2 formation through $\mathrm{CN} + \mathrm{N} \rightarrow \mathrm{N_2} + \mathrm{C}$ is suppressed by the competition with the $\mathrm{CN} + \mathrm{H_2} \rightarrow \mathrm{HCN} + \mathrm{H}$ reaction. The slow N_2 formation leads to more nitrogen being available for species beyond N_2, most notably HCN and NH_3. This also impacts the abundance of NO, which is formed less efficiently in the UV-shielding model and thus has a lower abundance (Figure 1).

NH_3 formation is initiated by the reaction of He^+ with N_2 or HCN, forming N^+. The addition reaction with H_2 allows for the eventual formation of NH_4^+, the precursor to NH_3. The main destruction channel for NH_3 in these hot layers is atomic H. Suppressing the photodissociation of H_2O lowers the production, and thus the abundance of atomic H. This increases the NH_3 lifetime and thus abundance as more hydrogen is available in the form of H_2. We see that NH_3 has a maximum abundance occurring at the water-ice line with the inclusion of UV shielding of roughly 10^{-7}, a value four orders of magnitude higher than when UV shielding is excluded.

Lastly, the active carbon chemistry allows for atomic nitrogen to react with the abundant carbon chains (C_xH, C_yN), which produces CN, which reacts with H_2 to form HCN. HCN can then react with the more abundant CH_3^+ to form CH_3CNH^+, the precursor for CH_3CN.

The only nitrogen species that has so far been observed in the inner disk is HCN. HCN has been observed with columns of $10^{14}-10^{15}$ cm^{-2} in Salyk et al. (2011b) and predicted to have columns of $10^{14}-10^{16}$ cm^{-2} in the line-forming region at 0.3 au by Woitke et al. (2018). Though the column by Woitke et al. (2018) matches the observation, their emission line is weaker, similar to the case of C_2H_2 as the column is built up within deeper, cooler gas. Higher HCN fluxes are only seen by letting the C/O ratio approach unity in Woitke et al. (2018). We produced a column of 10^{19} cm^{-2} with the effects of UV shielding included. This column has a strong contribution from warm surface layers (e.g., Figure 2 and thus the flux from our model is likely stronger than that with the C/O = 0.46 from Woitke et al. (2018).

The species that might be detectable are NO and NH_3 with columns of 5×10^{16} cm^{-2} and 3×10^{16} cm^{-2}, respectively, while it is less likely to observe CH_3CN with a column of 9×10^{14} cm^{-2}.

5. Conclusions

In this work, we have studied the effects of water UV shielding on the chemical compositions of the inner, planet-forming region of protoplanetary disks. Specifically, we are looking at chemical abundances in the upper disk atmosphere where the IR line emission originates and the effects of water UV shielding are most prominent. This is done in order to further our understanding of observed emission from organics, which will be critical for the interpretation of observations by the James Webb Space Telescope.

We have concluded that water self-shielding has notable effects for hydrocarbons and nitriles. The lack of OH produced by H_2O dissociation suppresses N_2, CO, and CO_2 formation.

As a result, there is more carbon and nitrogen available for a rich carbon and nitrogen chemistry (>3 orders of magnitude), boosting the abundance of C_2H_2, CH_4, HCN, CH_3CN, and NH_3.

The depletion seen in CO and CO_2 cannot be explained alone by the formation of species such as HCN, C_2H_2, CH_4, and CH_3CN. A significant amount (up to 53%) of the total volatile carbon finds its way into larger carbon chains, such as C_6H_2 and C_9H_2. The nitrogen released from N_2 finds its way to HCN with traces in CH_3CN and NH_3. We expect to observe CH_4, HCN, NO, and NH_3 with column densities shown in Figure 3.

The inclusion of water UV shielding provides a way to increase the production of C_2H_2 and HCN, which have been historically underproduced, without invoking a C/O ratio near unity. Model abundances for H_2O and CO_2 are already in agreement with observations, noted in Paper I and Paper III, thus this is a step forward in matching all four species at the same time.

Water UV shielding is important for the entire chemical inventory. Through its ability to both block UV rays from penetrating deep into the disk and to create an effectively oxygen-poor environment, formation conditions become more favorable for various hydrocarbons and nitriles. This work has shown that water UV shielding impacts the inner disk chemical composition and better reproduces observation. Thus, further studies that vary the C/O ratio with UV shielding are needed to advance our understanding of the inner disk chemistry and its evolution.

S.E.D, A.D.B. and E.A.B. acknowledge support from NSF Grant#1907653 and NASA grant XRP 80NSSC20K0259.

Software: astropy (Astropy Collaboration et al. 2013, 2018), SciPy (Virtanen et al. 2020), NumPy (van der Walt et al. 2011), Matplotlib (Hunter 2007).

Appendix
2D Structure Comparisons

Figure 4 shows the 2D structure of the gas temperature and density, dust density, gas-to-dust ratio, and UV and X-ray radiation fields for the model with water UV shielding. The UV radiation field is relative to the interstellar radiation field (Draine 1978). The red line at $z/r \sim 0.15$ signifies the lower bound of the IR-emitting layer. Figure 5 compares the 2D abundance structure of H_2O and CO_2 for a full chemical network, as employed in this work, and a reduced chemical network, used in Bosman et al. (2022a). We can see that for both the standard model and model with water UV shielding, the resulting abundances in our estimation of the IR-emitting layer for both species are independent of the chemical network used.

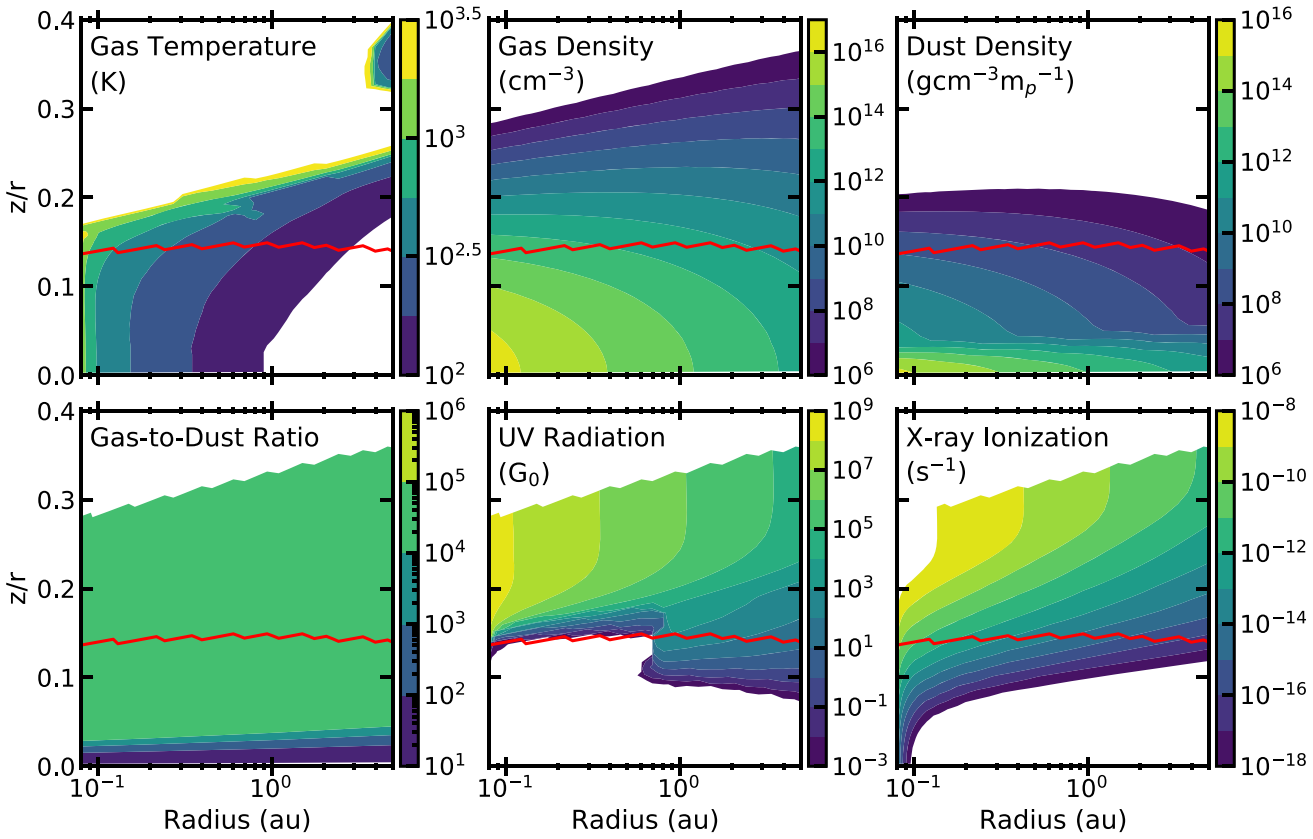

Figure 4. 2D distributions of the inner 5 au of the disk showing the structure of the gas temperature and density, dust density, gas-to-dust ratio, and UV and X-ray radiation fields for the model with water UV shielding. The UV radiation field is relative to the interstellar radiation field (Draine 1978). The red line at $z/r \sim 0.15$ signifies our estimation of the location of the IR-emitting layer.

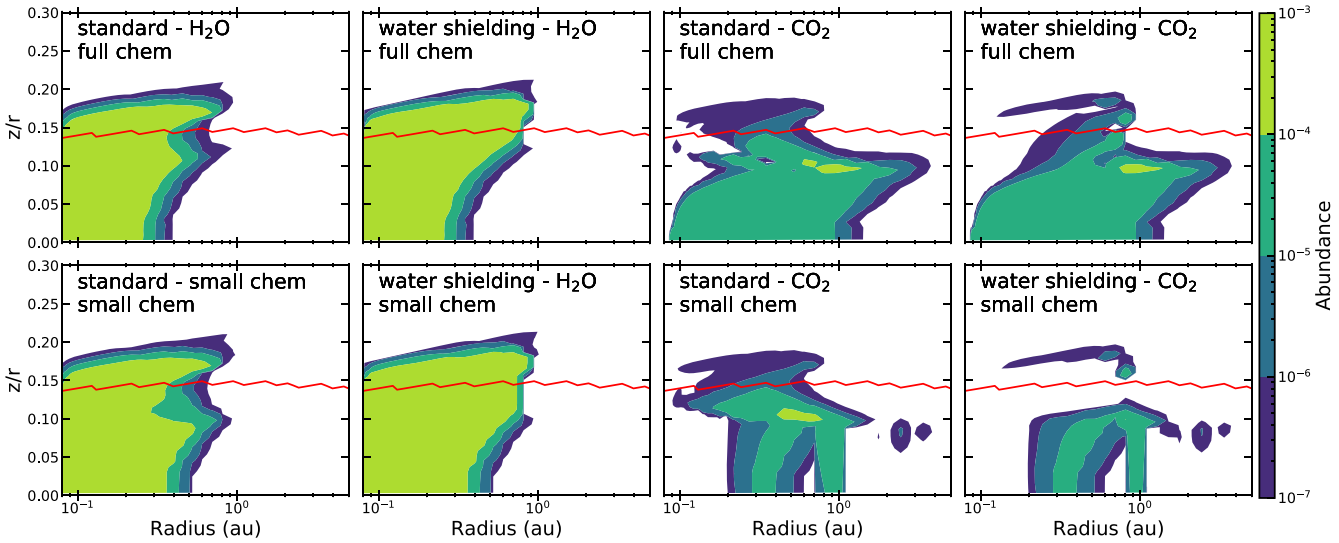

Figure 5. 2D distributions of water and CO_2 for a full and reduced chemical network shown in the top and bottom panels, respectively. The reduced chemical network is used in Bosman et al. (2022a). The region above the red line at $z/r \sim 0.15$ corresponds to the location of our estimation of the IR-emitting layer. For water, we can see specifically around 1 au near the IR-emitting layer that the model with UV shielding has a noticeably larger abundance than the standard model, as expected. For a reduced chemical network, the abundances drop at closer-in radii due to the fact that the water-ice lines are at smaller radii (Bosman et al. 2022a). We are focusing on the region in the IR-emitting layer, so between the models, the abundance is about the same, validating the use of a smaller chemical network to obtain the emitting area of water. For CO_2, we also see very similar abundances in the IR-emitting layer between a full and reduced chemical network.

ORCID iDs

Sara E. Duval https://orcid.org/0000-0003-0014-0508
Arthur D. Bosman https://orcid.org/0000-0003-4001-3589
Edwin A. Bergin https://orcid.org/0000-0003-4179-6394

References

Anderson, D. E., Blake, G. A., Cleeves, L. I., et al. 2021, ApJ, 909, 55
Banzatti, A., Pascucci, I., Bosman, A. D., et al. 2020, ApJ, 903, 124
Bethell, T., & Bergin, E. 2009, Sci, 326, 1675
Bosman, A. D., Alarcón, F., Bergin, E. A., et al. 2021, ApJS, 257, 7
Bosman, A. D., Bergin, E. A., Calahan, J., & Duval, S. E. 2022a, ApJL, 930, L26
Bosman, A. D., Bergin, E. A., Calahan, J. K., & Duval, S. 2022b, ApJL, 933, L40
Bosman, A. D., Tielens, A. G. G. M., & van Dishoeck, E. F. 2018, A&A, 611, A80
Brown, J. M., Pontoppidan, K. M., van Dishoeck, E. F., et al. 2013, ApJ, 770, 94
Bruderer, S. 2013, A&A, 559, A46
Bruderer, S., van Dishoeck, E. F., Doty, S. D., & Herczeg, G. J. 2012, A&A, 541, A91
Calahan, J. K., Bergin, E. A., & Bosman, A. D. 2022, ApJL, in press
Carr, J. S., & Najita, J. R. 2008, Sci, 319, 1504
Carr, J. S., Najita, J. R., & Salyk, C. 2018, RNAAS, 2, 169
Cleeves, L. I., Öberg, K. I., Wilner, D. J., et al. 2018, ApJ, 865, 155
Cockell, C. S., Bush, T., Bryce, C., et al. 2016, AsBio, 16, 89
Draine, B. T. 1978, ApJS, 36, 595
Du, F., & Bergin, E. A. 2014, ApJ, 792, 2
Glassgold, A. E., & Najita, J. R. 2015, ApJ, 810, 125
Heays, A. N., Bosman, A. D., & van Dishoeck, E. F. 2017, A&A, 602, A105
Herczeg, G. J., Wood, B. E., Linsky, J. L., Valenti, J. A., & Johns-Krull, C. M. 2004, ApJ, 607, 369
Hunter, J. D. 2007, CSE, 9, 90
Ida, S., Yamamura, T., & Okuzumi, S. 2019, A&A, 624, A28
Johnson, J. A., Aller, K. M., Howard, A. W., & Crepp, J. R. 2010, PASP, 122, 905
Jonkheid, B., Kamp, I., Augereau, J. C., & van Dishoeck, E. F. 2006, A&A, 453, 163
Lahuis, F., van Dishoeck, E. F., Boogert, A. C. A., et al. 2006, ApJL, 636, L145
Lingam, M., & Loeb, A. 2019, AJ, 157, 25
Madhusudhan, N. 2019, ARA&A, 57, 617
Madhusudhan, N., Piette, A. A. A., & Constantinou, S. 2021, ApJ, 918, 1
Mandell, A. M., Haynes, K., Sinukoff, E., et al. 2013, ApJ, 779, 128
Morbidelli, A., Lunine, J. I., O'Brien, D. P., Raymond, S. N., & Walsh, K. J. 2012, AREPS, 40, 251
Morbidelli, A., & Raymond, S. N. 2016, JGRE, 121, 1962
Mulders, G. D., Ciesla, F. J., Min, M., & Pascucci, I. 2015, ApJ, 807, 9
Mulders, G. D., Pascucci, I., Apai, D., & Ciesla, F. J. 2018, AJ, 156, 24
Najita, J. R., Carr, J. S., Pontoppidan, K. M., et al. 2013, ApJ, 766, 134
Najita, J. R., Carr, J. S., Salyk, C., et al. 2018, ApJ, 862, 122
Öberg, K. I., Boogert, A. C. A., Pontoppidan, K. M., et al. 2011, ApJ, 740, 109
Öberg, K. I., Guzmán, V. V., Walsh, C., et al. 2021, ApJS, 257, 1
Pierrehumbert, R., & Gaidos, E. 2011, ApJL, 734, L13
Pontoppidan, K. M., Blake, G. A., & Smette, A. 2011, ApJ, 733, 84
Pontoppidan, K. M., Salyk, C., Blake, G. A., et al. 2010, ApJ, 720, 887
Astropy Collaboration, Price-Whelan, A. M., Sipőcz, B. B., et al. 2018, AJ, 156, 123
Raymond, S. N., Kokubo, E., Morbidelli, A., Morishima, R., & Walsh, K. J. 2014, in Protostars and Planets VI, 914, ed. H. Beuther et al. (Tuscon, AZ: Univ. Arizona Press), 595
Astropy Collaboration, Robitaille, T. P., Tollerud, E. J., et al. 2013, A&A, 558, A33
Salyk, C., Blake, G. A., Boogert, A. C. A., & Brown, J. M. 2011a, ApJ, 743, 112
Salyk, C., Pontoppidan, K. M., Blake, G. A., Najita, J. R., & Carr, J. S. 2011b, ApJ, 731, 130
Salyk, C., Pontoppidan, K. M., Blake, G. A., et al. 2008, ApJL, 676, L49
van der Walt, S., Colbert, S. C., & Varoquaux, G. 2011, CSE, 13, 22
Virtanen, P., Gommers, R., Oliphant, T. E., et al. 2020, Nat. Methods, 17, 261
Walsh, C., Nomura, H., Millar, T. J., & Aikawa, Y. 2012, ApJ, 747, 114
Walsh, C., Nomura, H., & van Dishoeck, E. 2015, A&A, 582, A88
Wei, C.-E., Nomura, H., Lee, J.-E., et al. 2019, ApJ, 870, 129
Woitke, P., Kamp, I., & Thi, W.-F. 2009, A&A, 501, 383
Woitke, P., Min, M., Thi, W. F., et al. 2018, A&A, 618, A57
Yoshino, K., Esmond, J. R., Parkinson, W. H., Ito, K., & Matsui, T. 1996, CP, 211, 387
Zhang, K., Booth, A. S., Law, C. J., et al. 2021, ApJS, 257, 5